Author/s:
Zheng, F;Hall, CR;Angmo, D;Zuo, C;Rubanov, S;Wen, Z;Bradley, SJ;Hao, X-T;Gao, M;Smith, TA;Ghiggino, KP

Title:
A sandwich-like structural model revealed for quasi-2D perovskite films

Date:
2021-04-28

Citation:
Zheng, F., Hall, C. R., Angmo, D., Zuo, C., Rubanov, S., Wen, Z., Bradley, S. J., Hao, X. -T., Gao, M., Smith, T. A. & Ghiggino, K. P. (2021). A sandwich-like structural model revealed for quasi-2D perovskite films. Journal of Materials Chemistry C, 9 (16), pp.5362-5372. https://doi.org/10.1039/d1tc00606a.

Persistent Link:
https://hdl.handle.net/11343/337155

Journal of
Materials Chemistry C
Materials for optical, magnetic and electronic devices

This article can be cited before page numbers have been issued, to do this please use: F. Zheng, C. R. Hall, D. Angmo, C. Zuo, S. Rubanov, Z. Wen, S. Bradley, X. Hao, M. Gao, T. Smith and K. Ghiggino, *J. Mater. Chem. C*, 2021, DOI: 10.1039/D1TC00606A.

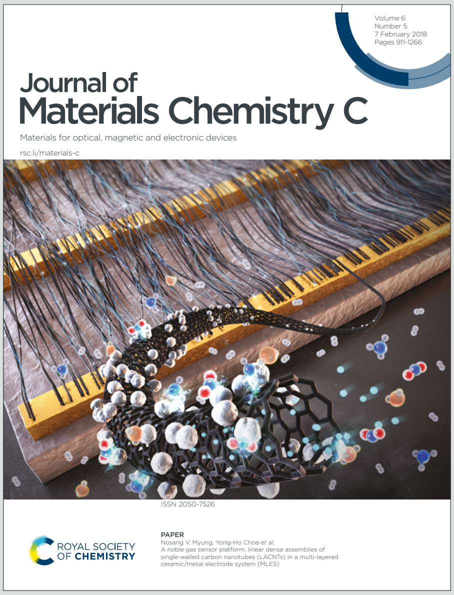

View Article Online
DOI: 10.1039/D1TC00606A

A Sandwich-Like Structural Model Revealed for Quasi-2D Perovskite Films

Fei Zheng,[a] Christopher R. Hall,[a] Dechan Angmo,[b] Chuantian Zuo,[b] Sergey Rubanov,[c] Zhenchuan Wen,[d] Siobhan J. Bradley,[a] Xiaotao Hao,[d] Mei Gao,[b] Trevor A. Smith,[a] and Kenneth P. Ghiggino*[a]

[a] *School of Chemistry and ARC Centre of Excellence in Exciton Science, The University of Melbourne, Parkville, Victoria 3010, Australia. Email: ghiggino@unimelb.edu.au*

[b] *Flexible Electronics Laboratory, CSIRO Manufacturing, Clayton, VIC 3168, Australia*

[c] *Advanced Microscopy Facility, Bio21 Institute, The University of Melbourne, Victoria 3010, Australia*

[d] *School of Physics, State Key Laboratory of Crystal Materials, Shandong University, Jinan 250100, Shandong, China*

† Electronic Supplementary Information (ESI) available. See DOI: xxx/xxx

Abstract

The excellent performance and stability of perovskite solar cells (PSCs) based on quasi-2D Ruddlesden-Popper perovskites (RPPs) holds promise for their commercialization. Further improvement in the performance of 2D PSCs requires a detailed understanding of the microstructure of the quasi-2D perovskite films. Based on scanning transmission electron microscopy (STEM), time-resolved photoluminescence, and transient absorption measurements, a new sandwich-like structural model is proposed to describe the phase distribution of RPPs. In contrast to the conventional gradient distribution, it is found that small-*n* RPPs are sandwiched between large-*n* RPP phase layers at the front and back sides owing to crystallization initiated from both interfaces during film formation. This sandwich-like distribution profile facilitates excitons funneling from the film interior to both surfaces for dissociation while free carriers transport *via* large-*n* channels that permeate the film to ensure efficient charge collection by the corresponding electrodes, which is favorable for high-performance photovoltaics. This discovery provides a new fundamental understanding of the operating principles of 2D PSCs and has valuable implications for the design and optimization strategies of optoelectronic devices based on quasi-2D RPPs films.

Introduction

Quasi-two dimensional (2D) Ruddlesden-Popper perovskites (RPPs) have emerged as excellent candidates for developing perovskite solar cells (PSCs) with enhanced moisture tolerance and suppressed ion migration compared to their 3D perovskite counterparts.[1-7] The structural formula of RPPs is given as $R_2A_{n-1}Pb_nX_{3n+1}$, where R is the alkyl or aromatic moiety terminated long-chain ammonium ligands, such as *n*-butylammonium ($BA^+=C_4H_9NH_3^+$) and phenethylammonium cations

View Article Online
DOI: 10.1039/D1TC00606A

($PEA^+=C_8H_9NH_3^+$), A is the short-chain ammonium cation (methylammonium, $MA^+= CH_3NH_3^+$), and X is the halide anion (Cl^-, Br^-, I^-).[1, 8] An individual RPPs slab is composed of *n* layers of 2D $[PbX_6]^{4-}$ octahedral sheets in the middle and two monolayers of long-chain ammonium ligands (R^+) on the edges,[9] as shown in Fig. 1a which depicts the structure of BA^+ based RPPs with slab thickness of *n*=3 and *n*=5 as an example. It can be regarded as a quantum-well (QW) owing to both the quantum and dielectric confinement brought about by the nm-scale width and the low conductivity spacer cations.[10] The optical properties of RPPs are determined by the slab thickness (*n*), exhibiting decreased energy bandgap (E_g) and decreased exciton binding energy (E_b) with increasing *n* value.[11] The feasibility of tuning *n* through stoichiometric control has led to applications of quasi-2D RRPs in narrowband photodetectors and highly efficient light-emitting diodes.[12, 13]

The scalable fabrication of RPP photovoltaic devices is most easily enabled by depositing quasi-2D perovskite films.[1, 2] Considering the insulating nature of long-chain ligands on both sides of the RPP slabs, the perpendicular alignment of RPPs ((010) lattice plane) relative to the substrate, and the electrodes, is crucial for achieving high charge carrier conductivity in the out-of-plane direction and this is key to achieving high-performance PSCs[2]. Fortunately, the orthogonal orientation of RPPs can be readily achieved either by spin-coating or drop-casting the precursor solutions on hot substrates, with the assistance of compositional control,[14, 15] solvent engineering,[16, 17] or additives doping.[18, 19] However, quasi-2D perovskite films cast from the RPPs precursor with a nominal *n* value (<*n*>) is not a simple assembly of the phase pure RPPs with the designated slab thickness <*n*> but rather a phase mixture of RPPs with thicknesses (*n*) distributed around <*n*>, from small-*n* to large-*n* and even a 3D-like component ($n=\infty$).[14, 20] This compositional inhomogeneity not only complicates the microstructure of the quasi-2D perovskite films but also hinders optimization of 2D PSCs where a precise energy bandgap diagram is demanded.

The spatial distribution of RPPs within quasi-2D perovskite films is still under debate and yet to be fully understood.[21, 22] A gradient distribution of RPPs in the out-of-plane direction with small-*n* (*n*=2, 3, 4, 5) components on the bottom and 3D-like component ($n=\infty$) on the top of the film has been proposed based on photoluminescence (PL) characterization.[20] High energy PL emission bands assigned to the small-*n* (*n*=2, 3, 4, 5) RPPs can be observed from the back side (perovskite/substrate interface) of the quasi-2D perovskite films while PL spectra collected from the front side (perovskite/air interface) mainly feature the low energy emission from 3D-like perovskite phases.[23] Lin et al.[22] proposed that the 3D-like phases are distributed throughout the quasi-2D perovskite film, forming a percolating network responsible for the carrier transport along the out-of-plane direction. Following photoexcitation, energy transfer, or exciton diffusion, occurring from the small-*n* RRPs to the large-*n* RRPs, that eventually funnels the energy to the 3D-like perovskite phase, has been suggested to occur in the quasi-2D perovskite films.[24, 25] Regardless of the wide acceptance of this gradient phase distribution model proposed for quasi-2D perovskite films, structural or spectral information from the

View Article Online
DOI: 10.1039/D1TC00606A

interior layer of the film to further support the structural model is lacking. Further investigation into the micro-structure and internal exciton dynamics of the quasi-2D perovskite film to obtain a more faithful structural model is thus warranted to better understand the mechanism of exciton transport and thus guide the optimization of 2D PSCs for achieving a higher PCE and improved stability.

Herein, we provide an in-depth investigation of $BA_2MA_{n-1}Pb_nI_{3n+1}$ ($<n>=5$) quasi-2D perovskite films prepared by the one-step drop-casting method,[26] including structural and spectral characterization. UV-Vis and grazing-incidence wide-angle X-ray scattering (GIWAXS) measurements confirm the multiphase nature of the quasi-2D perovskite film and the orthogonal orientation of the (010) lattice plane relative to the substrate for all RPP phases within this film. A sandwich-like distribution profile for RPP phases along the out-of-plane direction of the quasi-2D perovskite film, with the large-n ($n\approx25$) RPP phases occupying both the front and back sides of the film and the small-n (n=3, 4, 5) RPP phases comprising the lower middle part of the film, is proposed based on scanning transmission electron microscopy (STEM) and excitation intensity-dependent PL characterization. Femtosecond transient absorption (TA) analysis using both front- and back-side excitation further supports this sandwich-like structural model proposed for the quasi-2D perovskite film. This new structural model implies a fusiform-like energy bandgap diagram for the quasi-2D perovskite film, which would facilitate funneling of excitons from small-n RPPs inside the film towards the large-n phases located at both sides of the film, which ultimately can dissociate into free carriers to be collected by the electrodes in PSC devices. We suggest this sandwich-like structural model for the $BA_2MA_{n-1}Pb_nI_{3n+1}$ ($<n>=5$) quasi-2D perovskite film may be general for quasi-2D RPPs films prepared by other casting methods, such as spin-coating or scalable slot-die coating,[26] where hot substrates are often adopted.

Results and Discussion

High-performance 2D PSC devices based on the $BA_2MA_{n-1}Pb_nI_{3n+1}$ ($<n>=5$) quasi-2D perovskite film have been demonstrated by us previously by one-step drop-casting on hot substrates.[27] To exclude the influence of the substrate on the composition and structure of the quasi-2D perovskite, UV-Vis absorption measurements of the $BA_2MA_{n-1}Pb_nI_{3n+1}$ ($<n>=5$) films drop-cast on the bare glass substrate and the PEDOT:PSS (hole transporting polymer layer used in PSCs) coated glass substrate were conducted. The absorption spectra of the two samples (Fig. S1†, Electronic Supplementary Information), are almost identical, consisting of high energy absorption peaks of small-n (n=3, 4, 5) RPP phases and a low energy absorption band corresponding to the large-n (n=L) RPPs. To simplify the film interfacial conditions, the $BA_2MA_{n-1}Pb_nI_{3n+1}$ ($<n>=5$) quasi-2D perovskite film deposited on the bare glass substrate was selected for structural analysis.

The structures of $BA_2MA_2Pb_3I_{10}$ (n=3) and $BA_2MA_4Pb_5I_{16}$ (n=5) RPPs are schematically illustrated in Fig. 1a. The $[PbI_6]^{4-}$ slabs confined by BA^+ spacer layers propagate in the $\vec{a}\vec{c}$ plane, and stack in the $\vec{b}$ direction to form RPP phases.[9, 28] The scattering pattern of the GIWAXS image of the BA_2MA_{n-}

$_1$Pb$_n$I$_{3n+1}$ (<n>=5) quasi-2D perovskite film drop-cast on the glass substrate (Fig. 1b) exhibits indexed discrete Bragg spots consistent with literature reports,[2, 22, 26] indicating the high crystallinity and ordered texture of the layered perovskite film. The integral peak profile around $|q|$=10 nm^{-1} along the out-of-plane (q_z) direction (Fig. 1c) displays a strong diffraction peak at 9.08 nm^{-1} assigned to the (001) diffraction feature of PbI$_2$.[29] related to other structural features which we discuss later. As indicated by the green arrows, the scattering ring feature of the (001) peak in the GIWAXS image implies the random orientation of the PbI$_2$ crystalline domains. Based on the calculation provided in the ESI (Table S1†), the peak at 10.07 nm^{-1} is the ($\bar{1}1\bar{1}$) diffraction feature of the RPP with the thinnest slab thickness (n=3), while the feature centered at 9.95 nm^{-1} can be ascribed to the diffraction assembly from RPP phases of n>3, confirming the multi-phase nature of the quasi-2D perovskite film. The centralization of these ($\bar{1}1\bar{1}$) peaks in the q$_z$ direction indicates the orthogonal alignment of the (010) lattice plane relative to the substrate for all RPPs within the film.[22]

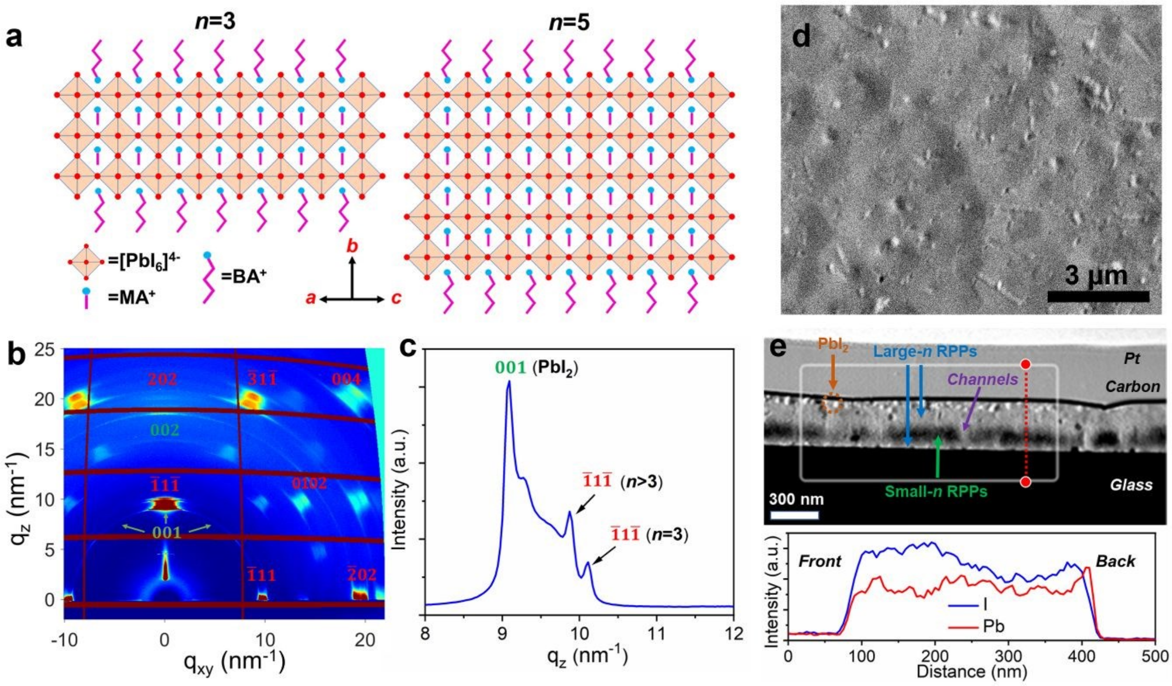

Fig. 1 Morphology and structural information. (a) Schematic structure of 2D BA$_2$MA$_{n-1}$Pb$_n$I$_{3n+1}$ RPPs with slab thicknesses of n=3 and n=5; (b) Labelled GIWAXS pattern of the drop-cast quasi-2D perovskite film; (c) The plotted profile of (001) and ($\bar{1}1\bar{1}$) diffraction peaks along the q_z direction; (d) Top-view scanning electron microscope (SEM) image of the drop-cast quasi-2D perovskite film; (e) The high-angle annular dark-field (HAADF) STEM image of the drop-cast BA$_2$MA$_{n-1}$Pb$_n$I$_{3n+1}$ (<n>=5) quasi-2D perovskite film lamella (upper panel) and the corresponding EDAX line scan profile of I and Pb along the labeled red dash line (lower panel).

The front surface morphology of the quasi-2D perovskite film was characterized by scanning electron microscopy (SEM). The top-view SEM image (Fig. 1d) shows that micrometer-sized (~2 μm) perovskite grains constitute the 2D layered perovskite film, which is similar to the morphology of 3D perovskite films.[30] To investigate the phase distribution of the quasi-2D perovskite film in the orthogonal direction, the cross-sectional image of the film was obtained by scanning transmission

View Article Online
DOI: 10.1039/D1TC00606A

electron microscopy (STEM). Perovskite lamella (~100 nm in thickness) with the structure of Glass/Quasi-2D Perovskite/Carbon/Pt for the measurement were prepared by the lift-off FIB (focused ion beam) technique (described in the Experimental Section and in Fig. S2†).[31] The high-angle annular dark-field (HAADF) STEM image of this lamella sample is shown in Fig. 1e, providing Z-contrast imaging scaling with the atomic number (Z).[32, 33] The high contrast between small-n (n=3) RPPs (average Z≈14.3) and large-n (n=50, for instance) RPPs (average Z≈20.9) enables the identification of a sandwich-like phase distribution profile wherein the dark phase layer in the lower-middle part of the quasi-2D perovskite film is composed of the small-n (n=3, 4, 5) RPPs and the light phase layers at the front and back sides of the film are the large-n RPPs. The atomic ratios of inorganic elements are lower in small-n RPPs than those in large-n RPPs, thus the iodine (I) distribution profile in the orthogonal direction revealed by the EDAX line scan (lower panel of Fig. 1e) features higher intensity at the front and back sides of the film, showing the enrichment of small-n RPPs in the lower-middle part of the film. This sandwich-like distribution profile of RPPs is further confirmed by the corresponding STEM-EDAX elemental mapping of iodine (I) and lead (Pb) in the rectangular area of Fig. 1e, as shown in Fig. S3a†. It should be noted that sections of the small-n layer are penetrated by the large-n RPPs (light color channels in Fig. 1e), making the film an imperfect "sandwich". To verify the influence of preparation methods on the proposed sandwich-like structure for quasi-2D perovskite films, the $BA_2MA_{n-1}Pb_nI_{3n+1}$ ($<n>$=5) film was prepared by spin-coating with anti-solvent on substrate at room temperature. The HAADF STEM image and the corresponding EDAX line scan of I and Pb for the spin-coated quasi-2D perovskite lamella (Fig. S3b†) depict a sequential phase distribution in the orthogonal direction, indicating that the sandwich-like phase structure of quasi-2D perovskite film is specific to preparation methods that use a hot substrate. The random texture that appears in Fig. S3b†, especially the dark phase in the lower part of the perovskite lamella, implies that small-n RPPs slabs within the spin-coated quasi-2D perovskite film are randomly oriented.

On the top of the RPP film, directly below the carbon layer, the HAADF image of the drop-cast quasi-2D perovskite lamella shows clusters, tens of nanometers in size, embedded in the front surface of the film (Fig. 1e). The brightest intensity of these clusters in the HADDF image indicates the highest average atomic number of these components. Considering the strong (001) diffraction peak of PbI_2 demonstrated in the GIWAXS result, these clusters embedded in the front surface can be identified as PbI_2 (average Z≈62.7) nanoclusters which are randomly oriented. It has been suggested that PbI_2 domains incorporated in the lead-halide perovskite film, especially in the film interface, can effectively passivate defect sites leading to improved performance of 3D PSCs.[34, 35] Thus, the PbI_2 nanoclusters formed on the front surface of the quasi-2D perovskite film are also likely to be beneficial for the performance of 2D PSCs.

Microscopic photoluminescence (PL) spectroscopic characterization of the $BA_2MA_{n-1}Pb_nI_{3n+1}$ ($<n>$=5) quasi-2D perovskite films drop-cast on the glass substrate was carried out from both sides of the film. The excitation laser was focused on the back (film/glass) or the front (film/air) surfaces (inset of Fig. 2a). Due to the high absorption coefficient of the film for the excitation wavelength and the self-absorption of the fluorescence by the film, PL collected in reflection mode can be ascribed to the RPPs near the film surface under low excitation intensity. The two normalized PL spectra collected from the front and back sides of the quasi-2D perovskite film under 400 nm laser excitation with 0.06 kW/cm^2 intensity (Fig. 2a) are almost identical and feature mainly the long-wavelength (low-energy) emission peak centered at 755 nm (1.642 eV), which can be attributed to radiative excitonic recombination in large-n RPPs, indicating sufficient exciton funneling from small-n RPPs to large-n RPPs under low fluence. The slab thickness, n, can be determined from the PL emission peak based on the empirical formula (Equation 1) proposed previously:[27]

$$E_x = 1.623\ eV + \frac{1}{0.063 \cdot n^2 + 0.458 \cdot n + 0.811}\ eV \tag{1}$$

where E_x ($E_x = E_g - E_b$) is the excitonic gap. The identical PL spectra recorded from the front and back surfaces indicate that large-n RPPs of $n \approx 25$ reside at the quasi-2D perovskite film interfaces. It should be noted that the slab thickness of large-n RPPs in the quasi-2D perovskite film is significantly less than that expected for $n = \infty$ (3D perovskite), thus rendering the film considerably moisture tolerant and resulting in the 2D PSC devices with high stability, which will be demonstrated later. Time-resolved PL (TRPL) measurements were carried out to compare the fluorescence decay profiles, which are the result of radiative recombination and trapping of carriers by surface defects in the large-n RPPs, collected from both sides of the film (Fig. 2b). Both decays are highly non-exponential and a 4-exponential function was used to parameterize the PL decay,[36] yielding amplitude-weighted PL lifetimes of 7.60 ns and 6.60 ns from the back and the front of the film, respectively. From the similarity of both the PL spectra and TRPL decays, it can be inferred that the large-n phases located in the front and back surfaces of the quasi-2D perovskite film are very similar in composition, possessing the same slab thickness ($n \approx 25$) and similar optical properties.

View Article Online
DOI: 10.1039/D1TC00606A

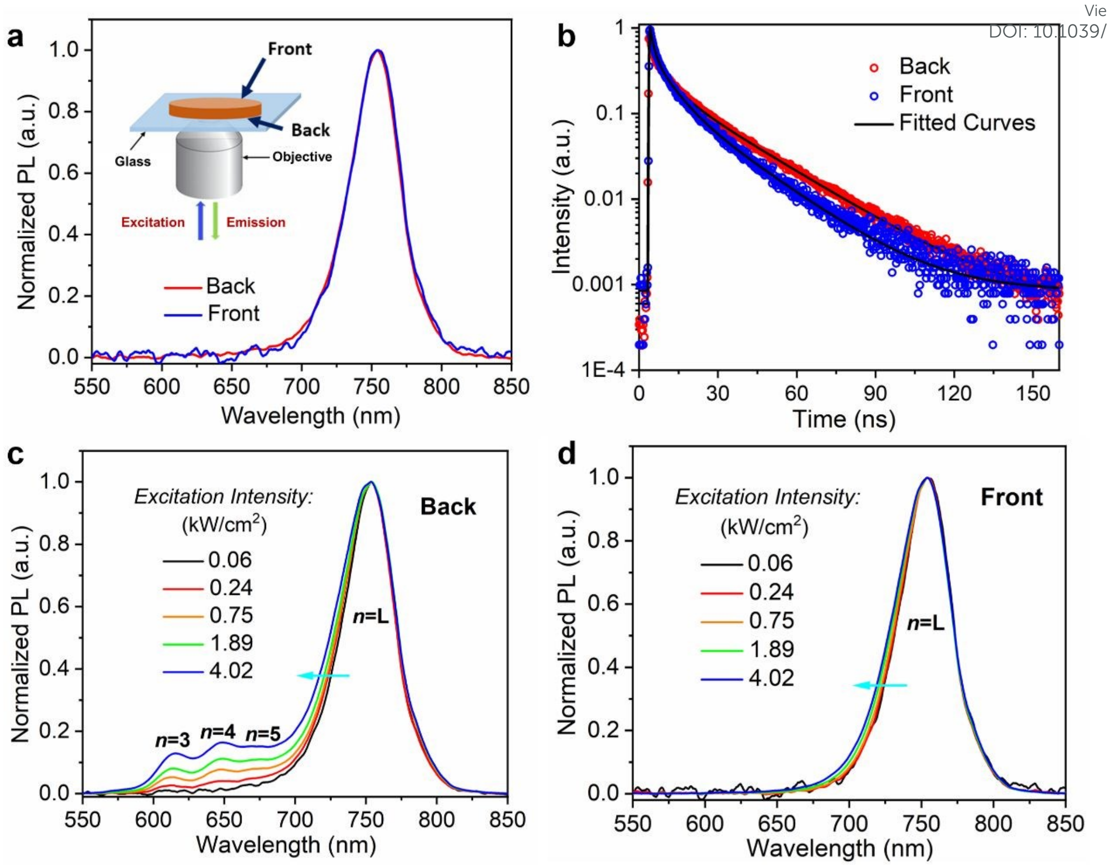

Fig. 2 (a) The PL spectra and (b) the TRPL decays collected from the back and front sides of the film on a glass substrate with low excitation intensity. (Excitation laser for PL: 400 nm, 5.4 MHz, 0.06 kW/cm^2; Excitation laser for TRPL: 400 nm, 1.0 MHz, 0.04 kW/cm^2; PL > 500 nm detected) The inset in (a) shows the schematic set-up adopted for both the PL and the TRPL measurements; Excitation intensity-dependent PL spectra collected from (c) the back-side and (d) the front-side of the film. (Excitation laser: 400 nm, 5.4 MHz.)

To gain further insight into the distribution of RPPs within the quasi-2D perovskite film, we performed intensity dependent PL measurements on both sides of the film. The intensity-dependent PL spectra collected from the back surface of the $BA_2MA_{n-1}Pb_nI_{3n+1}$ (<n>=5) film (Fig. 2c) show that when the intensity of the excitation laser is increased from 0.06 kW/cm^2 to 4.02 kW/cm^2, the short-wavelength PL emission peaks assigned to the small-n (n=3, 4, 5) RPPs phases emerge and increase relative to the long-wavelength PL peak of the large-n (n=L) RPPs. These observations can be well explained by the saturation of excited states in the large-n RPPs phase under high excitation fluence,[37] which impedes the exciton funneling from small-n to large-n and thus facilitate the excitonic recombination in small-n RPPs. By contrast, emission from the small-n RPPs (n=3, 4, 5) do not appear in the PL spectra from the front-side excitation even under 4.02 kW/cm^2 laser excitation power (Fig. 2d). The broadening of the long-wavelength PL peak (large-n RPPs) towards shorter wavelengths with increased excitation intensity can be observed from both front- and back-side excitation, indicating the existence of intermediate phases (5<n<25). This is consistent with the proposed sandwich-like phase distribution model where the small-n RPPs phase layer is located closer to the back surface of quasi-2D perovskite film. As the large-n RPPs phase layer near the back surface responsible for PL emission is thin and more excitons are generated in the small-*n* RPPs phases, large-*n* RPPs are more easily being saturated with back-side excitation. A similar dependence of PL spectra on the excitation intensity is observed for the $BA_2MA_{n-1}Pb_nI_{3n+1}$ (<*n*>=5) quasi-2D perovskite films deposited on the PEDOT:PSS coated substrate (Fig. S4a, b†) and the *iso*-Butylammonium (iBA) based $iBA_2MA_{n-1}Pb_nI_{3n+1}$ (<*n*>=5) quasi-2D perovskite films drop-cast on glass substrates (Fig. S4c, d†), implying the sandwich-like structure is also applicable to the 2D PSC device structures and can be generalized to other quasi-2D perovskite films.

The proposed sandwich-like structural model for the quasi-2D perovskite film was further verified by ultrafast transient absorption (TA) spectroscopy. Fig. 3a, b presents the 2D pseudocolor plots of the TA spectra (*m*ΔOD: pump-induced absorbance change) measured following 525 nm pulsed laser excitation (96 kHz, 1.6 μJ/cm^2) for the quasi-2D perovskite film obtained under both front- and back-side excitation (transmitted probe detection) modes. Distinct ground-state bleaching (GB) peaks corresponding to the *n*=3 (605 nm), *n*=4 (645 nm), and *n*=5 (670 nm) RPPs phases dominate the TA spectra obtained by back-side excitation at early pump-probe delays (0~5 ps). For the front-side excitation case, the GB peak assigned to the large-*n* (*n*=L) RPPs (735 nm) is the strongest GB peak over the entire decay range. This observation is more clearly demonstrated in Fig. 3c, d, where TA spectra at selected pump-probe delay times are presented. The difference between front and back excitation is consistent with the PL results and the asymmetric distribution of RPPs within the film. In contrast to the fixed positions for GB peaks of the small-*n* RPPs, the GB peak positions of the large-*n* RPPs obtained from both excitation modes red-shift during the 0~100 ps timescale and finally stabilize at ~735 nm. This red-shift can be explained by the coexistence of the large-*n* RPPs (lowest bandgap) and the intermediate RPPs phases in the quasi-2D perovskite film, wherein the excitons diffuse from the latter to the former after photo-excitation of the film by the pump pulse. For comparison, the TA characterization was applied to spin-coated quasi-2D perovskite films. The small difference between the TA spectra obtained by back- and front-side excitation (Fig. S5a, b, c†) indicates that RPPs are more uniformly distributed spatially in the orthogonal direction.

View Article Online
DOI: 10.1039/D1TC00606A

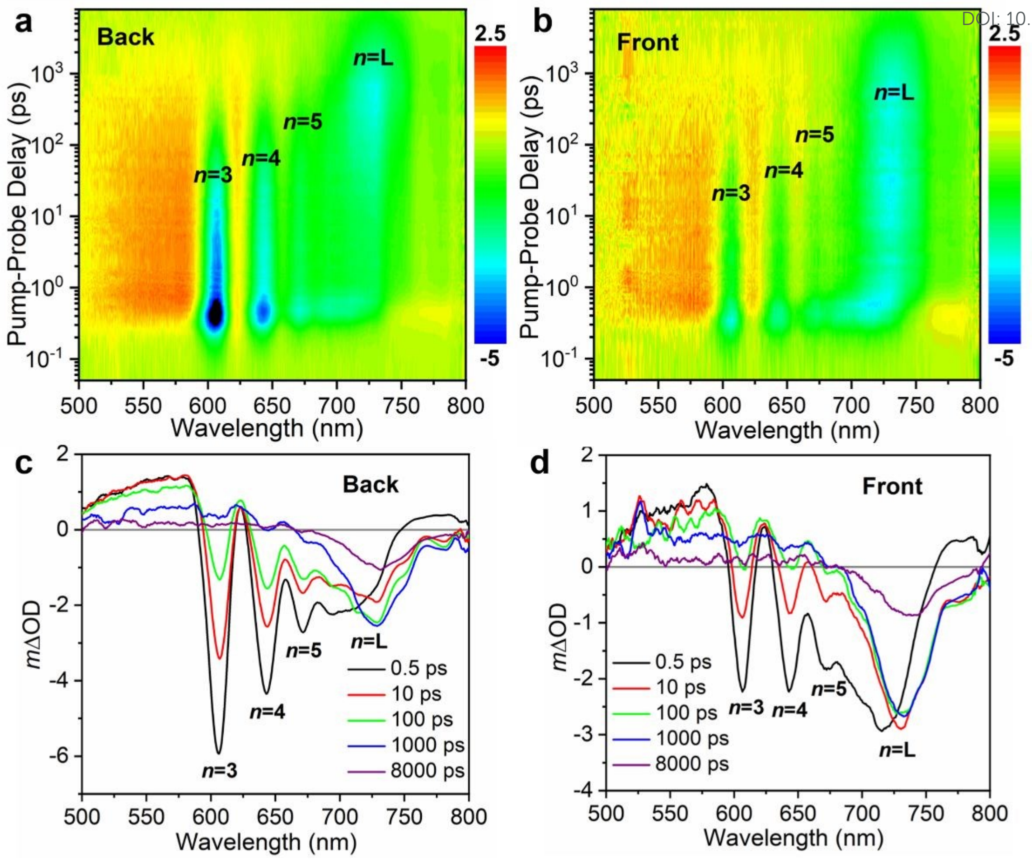

Fig. 3. TA characterization with back- and front-side excitation. Pseudo-color 2D plots of TA spectra ($m\Delta$OD) of the quasi-2D perovskite film obtained under (a) back- and (b) front-side excitation; TA spectra of the quasi-2D perovskite film as a function of probe wavelength recorded at various pump-probe delays obtained with (c) back- and (d) front-side excitation. (Pump laser: 525 nm, 96 kHz, 1.6 μJ/cm^2.)

To obtain the exciton dynamics within the quasi-2D perovskite film, TA signals of each of the GB peaks (-$m\Delta$OD) as a function of pump-probe delay obtained for front- and back-side excitation are plotted in Fig. 4a, b, c. The decay curves for the n=3, n=4, and n=5 GB peaks all feature a sub-picosecond decay component followed by a longer-lived component decaying on the hundreds-of-picoseconds timescale. The kinetic profiles for the GB peaks of the large-n (n=L) RPPs under both excitation modes are composed of both a rising component and a nanosecond scale slow decay channel. A bi-exponential decay function expressed by:

$$I(t) = I_0 + A_1 \exp\left(-\frac{t-t_0}{\tau_1}\right) + A_2 \exp\left(-\frac{t-t_0}{\tau_2}\right) \tag{2}$$

is applied to fit all the decay profiles, with fitting parameters summarized in Table 1. The lifetime for the fast decay component (τ_1) fit to all small-n RPPs was found to be ~0.35 ps, regardless of the excitation direction, which can be attributed to exciton-exciton annihilation.[38] The slower decay channel (τ_2) for excitons in the small-n RPPs can be assigned to a combined process of radiative recombination and interphase exciton transfer. For both the front- and back-side excitation modes, the gradual increase of τ_2 with the increase of n is suggestive of a sequential exciton transfer process where excitons are

View Article Online
DOI: 10.1039/D1TC00606A

step-wise funneled from small-*n* to larger-*n* phases, i.e. 3-to-4, 4-to-5. The relatively smaller τ_2 obtained using front-side compared to back-side excitation for all the small-*n* RPPs implies the interphase exciton transfer makes a weaker contribution to the observed kinetics. This can be explained by fewer excitons being generated in the small-*n* phases due to stronger attenuation of pump laser intensity passing through a thicker large-*n* RPPs phase layer on the front side of the film. Likewise, the exciton transfer from *n*=5 RPPs to the intermediate RPPs phases, and finally being funneled to the large-*n* RPPs (lowest bandgap), should be more prominent under the back-side excitation mode than the front-side excitation. This proposal is confirmed by the greater contribution and slower rise of the large-*n* GB peak (-*m*ΔOD) under the back-side excitation (rise time τ_1=107±9 ps, contribution~38.6%) compared to front-side excitation (τ_1=12±3 ps, contribution~11.7%). Interestingly, although the initial ground state transient bleaching (units of -*m*ΔOD) of the large-*n* GB peak after photo-generation and thermal relaxation of excitons (~0.5 ps) obtained using the back-side excitation mode (~1.7) and the front-side excitation mode (~2.4) are different (Fig. 4c), they reach a similar value (~2.9) after completion of the exciton funneling to the lowest energy (large-*n* RPPs) phase. Thus, the final population of excitons (or dissociated free carriers) harvested by the large-*n* RPPs in the quasi-2D perovskite film is independent of the incident light direction, despite the asymmetrical phase distribution profile of RPPs within the film. For this to occur, the interphase transfer of excitons must be highly efficient.

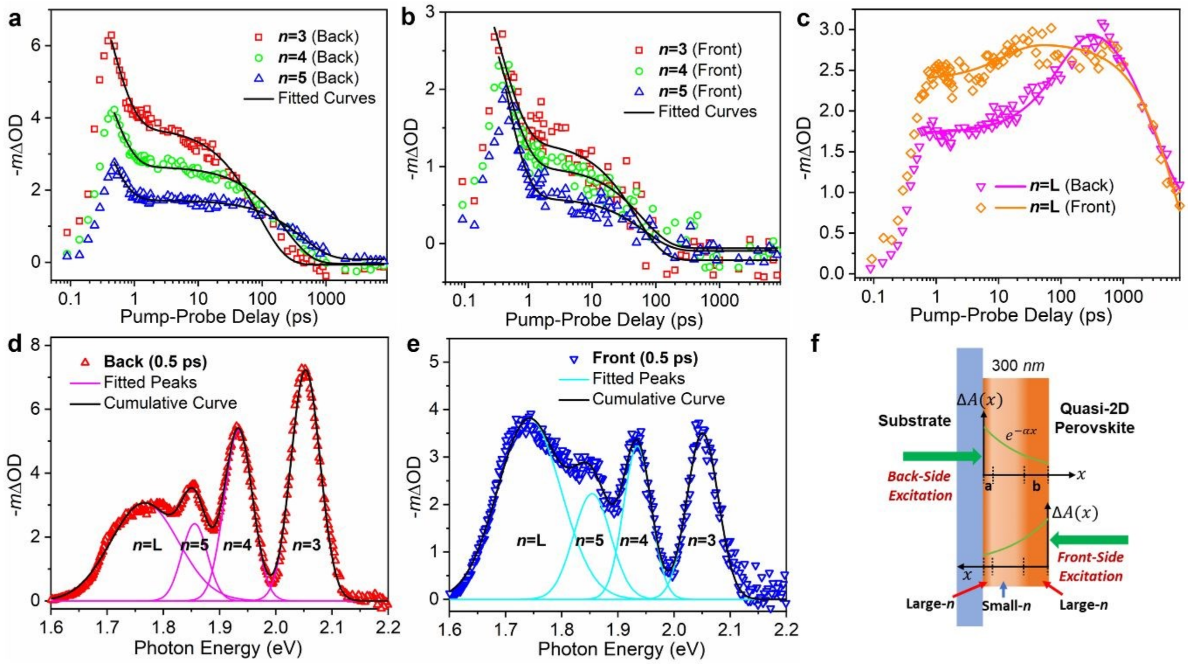

Fig. 4. Exciton dynamics and the phase layer thickness calculation. Decay profiles and corresponding fitted curves of the GB peaks (-*m*ΔOD) of the small-*n* (*n*=3, 4, 5) RPPs as a function of pump-probe delay for the $BA_2MA_{n-1}Pb_nI_{3n+1}$ (<*n*>=5) quasi-2D perovskite film obtained using (a) back- and (b) front-side excitation modes; (c) Equivalent decay profiles for the large-*n* (*n*=L) RPPs. Gaussian peak-fitted TA spectra (0.5 ps pump-probe delay) plotted as a function of photon energy obtained with (d) back- and (e) front-side excitation; (f) Schematic of the simplified structural model of the quasi-2D perovskite film used for the calculation of phase layer thickness.

View Article Online
DOI: 10.1039/D1TC00606A

Table 1. Fitting parameters for decay profiles of indicated GB peaks (-*m*ΔOD) obtained from back- and front-side excitation, applying a bi-exponential decay function.

		A_1	τ_1 (ps)	A_2	τ_2 (ps)
***n*=3**	Front	1.49±0.14 (49.3%)	0.35±0.07	1.53±0.07 (50.7%)	50±7
	Back	2.42±0.13 (40%)	0.38±0.04	3.79±0.07 (60%)	87±5
***n*=4**	Front	1.43±0.09 (57.7%)	0.40±0.05	1.05±0.05 (42.3%)	62±10
	Back	1.49±0.08 (35.6%)	0.35±0.03	2.69±0.04 (64.4%)	223±12
***n*=5**	Front	1.05±0.08 (60.3%)	0.35±0.04	0.69±0.04 (39.7%)	68±13
	Back	1.05±0.06 (39.2%)	0.30±0.03	1.63±0.03 (60.8%)	430±26
***n*=L**	Front	-0.43±0.04 (11.7%)	12±3	3.24±0.03 (88.3%)	7900±400
	Back	-1.49±0.06 (38.6%)	107±9	2.37±0.11 (61.4%)	3200±500

Table 2. Fitting parameters for TA spectra (0.5 ps pump-probe delay) obtained from back- and front-side excitation using Gaussian function fitting.

	Back		Front	
	Position (*eV*)	Area (relative contribution)	Position (*eV*)	Area (relative contribution)
***n*=3**	2.05	0.47 (**33.4%**)	2.05	0.25 (**21.0%**)
***n*=4**	1.93	0.33 (**23.8%**)	1.93	0.20 (**17.1%**)
***n*=5**	1.85	0.14 (**9.8%**)	1.85	0.19 (**15.8%**)
***n*=L**	1.77	0.46 (**32.9%**)	1.74	0.54 (**46.1%**)

As the concentration of photo-generated excitons in each RPPs phase is proportional to the corresponding optical absorbance, TA spectra at 0.5 ps pump-probe delay, just after photo-excitation and the exciton cooling processes, obtained from both the back- and front-side excitation modes are selected to further analyze the phase distribution information of the quasi-2D perovskite film. For simplicity, the large-n RPPs (lowest bandgap) and the intermediate RPP phases are regarded as one in this analysis, nominally labeled as large-*n* (*n*=L) RPPs. The baseline-corrected TA signals (-*m*ΔOD) plotted as a function of the photon energy were fit by GB peaks corresponding to the small-*n* (*n*=3, 4, 5) and the large-*n* (*n*=L) RPPs using Gaussian functions (Fig. 4d, e). Fitting parameters including the peak position, peak intensity (area integral), and the corresponding weight ratio are summarized in Table 2. The fitted peak positions of *n*=3, *n*=4, and *n*=5 RPPs from the two excitation modes are identical. By contrast, the fitted GB peak position of *n*=L RPPs obtained from the back-side excitation (1.77 eV) is larger than that from the front-side excitation (1.74 eV), indicating more intermediate RRP phases (possessing a higher bandgap than the large-*n* RPPs) are photo-excited by the pump pulse using

View Article Online
DOI: 10.1039/D1TC00606A

the back-side excitation mode. To quantitively compare the layer thickness of the large-*n* RPPs phase on the back and the front side of the quasi-2D perovskite film, a simplified structural model containing only the large-*n* RPPs on both sides and the small-*n* RPPs in the middle is constructed, as illustrated in Fig. 4f. The absorption coefficient (α) for both phases at the pump-laser wavelength (525 nm) is estimated as $4.9 \times 10^{-3}\ \mathrm{nm}^{-1}$ based on the UV-Vis absorption spectra (Fig. S1†) and the film thickness is ~300 nm obtained from the STEM image, given the absorption profile of the pump laser expressed as $\Delta A(x) = \alpha \cdot \exp(-\alpha x)$ (Fig. 4f).[39] Assuming the layer thicknesses of the large-*n* RPP phase on the back and the front sides of the film to be a and b, respectively, the following formulae apply:

$$\frac{\int_0^a e^{-\alpha x}dx + \int_{300-b}^{300} e^{-\alpha x}dx}{\int_a^{300-b} e^{-\alpha x}dx} = 0.490 \tag{2-a}$$

$$\frac{\int_0^b e^{-\alpha x}dx + \int_{300-a}^{300} e^{-\alpha x}dx}{\int_b^{300-a} e^{-\alpha x}dx} = 0.855 \tag{2-b}$$

In these formulae, the numerical values 0.490 and 0.855 refer to the relative weight ratio of the *n*=L GB peak intensity (integrated area) to the total intensity of the *n*=3, 4, 5 GB peaks calculated for the back- and front-side excitation modes, respectively. The numerical solution gives a = 33 nm and b = 77 nm, demonstrating that the large-*n* RPPs phase layer on the back side of the quasi-2D perovskite film is much thinner than the large-*n* layer located on the front side of the film ($a<b$). Since the total film thickness is ~300 nm (STEM image Fig. 1e), the thickness of the small-*n* phase layer sandwiched in the film would be ~190 nm. Although there may be some discrepancy between these calculated layer thicknesses and the actual values due to the simplifications used in the analysis, the consistency between this calculated result and the structural information provided by the STEM image further supports the validity of the proposed sandwich-like structural model.

The advantage of the sandwich-like structure for quasi-2D perovskite films over other phase distribution profiles is identified by studies of PSCs. Fig. 5a shows the *J-V* curves of champion PSCs based on $BA_2MA_{n-1}Pb_nI_{3n+1}$ ($<n>=5$) quasi-2D perovskite films prepared by spin-coating (SC) on substrate at room temperature and by one-step drop-casting (DP) on the hot substrate, respectively. As summarized in the inset, the performance of the DP-PSC is substantially greater than SC-PSC, with respective highest PCE of ~12.8% compared to ~3.5%, for an active area of 0.2 cm². The statistics of PCE distribution for both SC- and DP-PSCs are shown in Fig. S6†. The short circuit current density (J_{SC}) and Fill Factor (FF) of the DP-PSC is substantially higher than that of the SC-PSC. This is ascribed to the poor charge transport in the SC-film correlated with the random orientation of RPPs. Series resistance (R_S) and shunt resistance (R_{SH}) estimated from the *J-V* curves shows a much higher R_S value

View Article Online
DOI: 10.1039/D1TC00606A

for the SC-PSC (41.2 Ω·cm^2) than that of the DP-PSC (8.7 Ω·cm^2) while R_{SH} values are comparable, confirming poor charge-transport in the SC-PSC. Thus, better charge transport and collection in drop-cast quasi-2D perovskite films with the sandwich-like structure leads to a higher PCE for the DP-PSC. As shown in the inset of Fig. 5a, the DP-PSC retained 96.7% of its initial PCE after 500 hours under maximum power point tracking at constant AM1.5G solar illumination, demonstrating the superior performance stability of 2D PSCs comprised of large-*n* RPPs (*n*≈25) at the surface of quasi-2D perovskite films. The high external quantum efficiency (EQE) value (~80%) over the visible range for DP-PSC, Fig. S7†, confirms the photocurrent contribution from both the small-*n* and large-*n* RPPs during device operation. This is in good agreement with the highly efficient inter-phase exciton funneling from the small-*n* RPPs sandwiched in the film interior to the large-*n* RPPs at the film surfaces as revealed by the TA measurements.

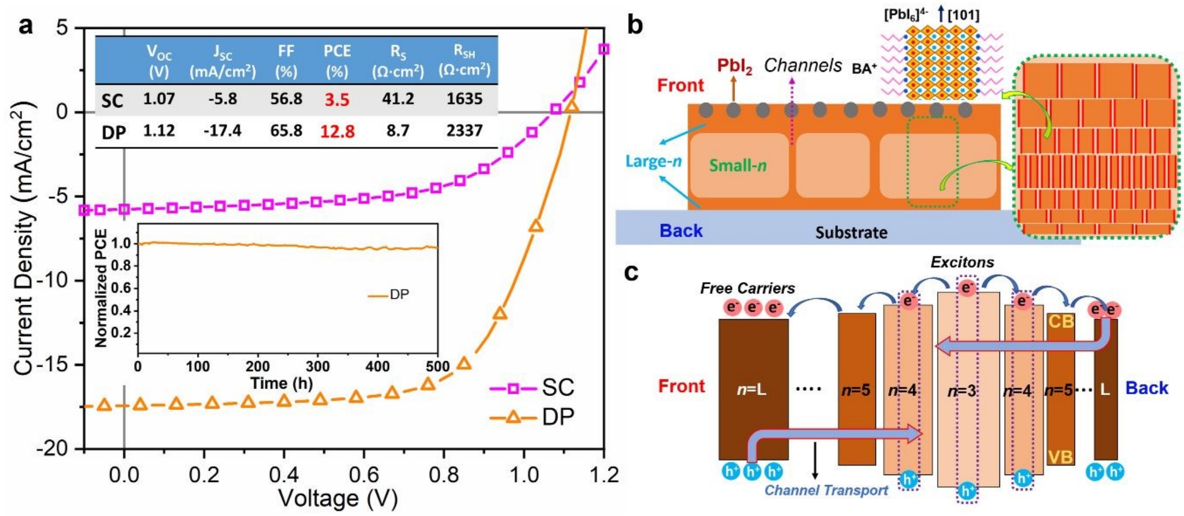

	V_{OC} (V)	J_{SC} (mA/cm^2)	FF (%)	PCE (%)	R_S (Ω·cm^2)	R_{SH} (Ω·cm^2)
SC	1.07	-5.8	56.8	3.5	41.2	1635
DP	1.12	-17.4	65.8	12.8	8.7	2337

Fig. 5 (a) Device performance of PSCs based on quasi-2D perovskite films prepared by spin-coating (SC) and drop-casting (DP) methods; Schematic illustration of (b) the sandwich-like structural model and (c) the fusiform-like bandgap diagram of the drop-cast $BA_2MA_{n-1}Pb_nI_{3n+1}$ (<*n*>=5) quasi-2D perovskite film.

Based on the above micro-structural and spectroscopic characterization results, we can detail the sandwich-like structural model for the drop-cast $BA_2MA_{n-1}Pb_nI_{3n+1}$ (<*n*>=5) quasi-2D perovskite film as follows. This quasi-2D perovskite film is composed of a mixture of RPPs phases with the $[PbI_6]^{4-}$ slab thickness (*n*) varying from the small-*n* (*n*=3, 4, 5) to large-*n* (*n*≈25). These RPP phases are perpendicularly aligned to the substrate, ensuring facile exciton diffusion in the out-of-plane direction required for high-performance 2D PSCs. As illustrated in Fig. 5b, the small-*n* (*n*=3, 4, 5) RPPs phase layers are located in the lower middle part of the quasi-2D perovskite film, while thin and thicker large-*n* (*n*≈25) RPP phase layers occupy the back (film/substrate) and front (film/air) sides of the film, respectively. The large-*n* RPPs and the small-*n* RPPs are connected by intermediate RPP phases (5<*n*<25) for both sides of the film. The PbI_2 nanoclusters embedded in the front surface of the quasi-2D perovskite film are beneficial for the performance of the 2D PSCs by providing efficient defect-sites passivation. Considering the type-I heterojunction formed between different $BA_2MA_{n-1}Pb_nI_{3n+1}$

RPPs as revealed recently by ultraviolet photoelectron spectroscopy (UPS),[25] a fusiform-like bandgap diagram for the quasi-2D perovskite film can be implied, as schematically depicted in Fig. 5c. This bandgap structure would facilitate the diffusion of photo-generated excitons towards the large-*n* (n≈25) RPP phases at the film surfaces where they can readily dissociate into free carriers to be collected by electrodes in PSCs owing to the small exciton binding energy (E_b) of the large-*n* RPPs. Similar behavior of excitons was previously attributed to the presence of lower-energy layer-edge states (LESs) at the surface of quasi-2D perovskite films, which rationalized the observed PCE of solar cell devices.[40] In addition, the small portion of large-*n* RPPs phase penetrating through the film can act as fast channels for transporting dissociated free carriers to the corresponding electrodes (indicated as “Channel Transport” in Fig. 5c), avoiding possible energy barriers associated with the larger-bandgap small-*n* RPPs inside the films. All these factors are advantageous to achieve a high PCE for 2D PSCs.

Very recently, Wang et al.[41] have proposed that the initial crystallized 3D-like perovskite at the liquid-air interface (front surface) templates the downwards growth of the small-*n* RPPs with orthogonal orientation during the formation of the quasi-2D perovskite film by spin-coating the precursor solution on a hot substrate (65 °C). Based on our model, we propose crystallization is initiated from both sides of the quasi-2D perovskite film cast from the precursor solution on a hot substrate. During the high temperature-induced fast solvent evaporation and the creation of solute supersaturation, crystallization of the orthogonally orientated large-*n* RPPs phase at both the liquid-air interface (front surface) and the liquid-substrate interface (back surface) initially takes place arising from substantial nuclei formation at both interfaces associated with the high surface energy.[42] These large-*n* phases template the subsequent growth of the orthogonally orientated RPPs with gradually decreased slab thickness (n) towards the center of the film at different rates, leading to an asymmetric sandwich-like RPPs phase distribution along the out-of-plane direction within the quasi-2D perovskite films. For quasi-2D perovskite films spin-coated on the cold substrate, large-*n* RPPs formation caused by the anti-solvent is only initiated from the front surface, leading to the random orientation of RPPs especially in the lower part of the film. These understandings might offer guidance for manipulating the thickness ratio between each large-*n*/small-*n* RPP phase layers to optimize the performance of quasi-2D perovskite-based optoelectronic film devices by altering the substrate temperature or controlling other environmental factors during the film preparation.

Conclusion

In conclusion, we have provided an in-depth investigation of the $BA_2MA_{n-1}Pb_nI_{3n+1}$ ($\langle n\rangle=5$) quasi-2D perovskite films, using structural and photophysical characterization techniques. A sandwich-like distribution profile for RPPs phases along the out-of-plane direction of the quasi-2D perovskite film, with the large-*n* (n≈25) RPP phase occupying the front and back sides of the film and the small-*n* (n=3, 4, 5) RPP phases being located in the lower middle part of the film, has been revealed for the first time. Both the excitation intensity-dependent PL spectra collected from both sides of the film and the

View Article Online
DOI: 10.1039/D1TC00606A

observed red-shift of the GB peak corresponding to large-n RPPs over a prolonged pump-probe delay time in the TA spectra indicate the existence of intermediate RPP phases ($5<n<25$) at both sides of the film, which bridge the large-n and the small-n RPP phase layers. A quantitative analysis based on the TA spectra leads to the conclusion that the large-n RPPs phase layer on the back side of the quasi-2D perovskite film is much thinner than that on the front side of the film, which is consistent with results from the STEM and the excitation intensity-dependent PL measurements. We suggest that the sandwich-like distribution (large-n/small-n/large-n) of the RPP phase layers arises from crystallization at both sides during film formation leading to a fusiform-like bandgap diagram for the quasi-2D perovskite films. This structure can facilitate excitons being funneled from the interior small-n (n=3, 4, 5) RPPs towards the large-n ($n\approx25$) RPP phases at the film surfaces where they can readily dissociate into free carriers to be collected by corresponding electrodes assisted by transport through large-n channels that penetrate through the film structure. These results not only provide new insight into the structure of the quasi-2D perovskite films, but also pave the way towards further optimization of the performance of quasi-2D perovskite-based optoelectronic devices by rationally manipulating the thickness ratio of each RPP phase layer within the films.

Experimental section

Materials

Lead iodide (PbI_2) was purchased from Alfa Aesar. Methylammonium iodide (MAI), *n*-butylammonium iodide (BAI), *iso*-butylammonium iodide (iBAI), methylammonium chloride (MACl), were provided by Greatcell Solar. Poly(3,4-ethylene dioxythiophene) polystyrene sulfonate (PEDOT:PSS) aqueous solution (Baytron P A1 4083) was purchased from HC Starck. All chemicals were used as received without further purification.

Film preparation

2.4 mmol PbI_2, 0.96 mmol BAI (or iBAI), 1.92 mmol MAI were dissolved into 2 ml DMF with magnetic stirring on a 70 °C hot plate for 30 mins, forming a 1.2 M (with respect to Pb^{2+}) stock precursor solution of the $BA_2MA_{n-1}Pb_nI_{3n+1}$ (or $iBA_2MA_{n-1}Pb_nI_{3n+1}$) ($\langle n\rangle=5$) perovskite. 100 μL perovskite precursor (1.2 M) and 72 μL MACl (0.1 M) and 228 μL pure DMF are mixed to produce the 6 mol% MACl doped $\langle n\rangle=5$ perovskite precursor (0.3 M). The $BA_2MA_{n-1}Pb_nI_{3n+1}$ ($\langle n\rangle=5$) quasi-2D perovskite films were deposited from these precursor solutions by the one-step drop-casting method.[26] 5 μL precursor was dropped onto the center of a UV-ozone treated clear glass substrate (2.5 cm × 2.5 cm), which was placed on a 60 °C hot plate, and spread out to form a circular film after the evaporation of DMF. Afterwards, the film was transferred to a 100 °C hot plate for 2 minutes of annealing. As reference samples, $BA_2MA_{n-1}Pb_nI_{3n+1}$ ($\langle n\rangle=5$) quasi-2D perovskite films drop-cast on the PEDOT:PSS coated glass substrates (2.5 cm × 2.5 cm) and $iBA_2MA_{n-1}Pb_nI_{3n+1}$ ($\langle n\rangle=5$) quasi-2D perovskite films on bare glass substrates were prepared following the same procedure. 6 mol% MACl doped $\langle n\rangle=5$ perovskite precursor with a concentration of 0.9 M was adopted for preparing spin-coated film samples.

View Article Online
DOI: 10.1039/D1TC00606A

Accordingly, 50 µl of the precursor solutions were spin-coated on top of the clear glass substrate at 1000 rpm for 10 s and 3500 rpm for 35 s, and 400 µl of ethyl acetate was dropped onto the film during the second stage, followed by annealing at 100 °C for 2 min.

Device fabrication and characterizations

Quasi-2D perovskite films for solar cell device fabrication were deposited by the one-step drop-casting (DP) method or spin-coating (SC) with anti-solvent. PSCs with the structure of ITO/PEDOT: PSS/Layered Perovskite/PCBM/PEIE/Ag and active area of 0.2 cm^2 were fabricated according to the procedure detailed in our previous work.[27] Current density-Voltage (*J-V*) curves of PSCs based DP- and SC-quasi-2D perovskite films were measured using a Keithley 2400 Source Meter with the scan rate of 30 mV/s under standard solar illumination (AM 1.5G, 100 mW·cm^{-2}). Stability tests of the encapsulated PSCs were conducted using the Candlelight Maximum Power Tracker.

General characterization

The UV−Vis absorption spectra of the $BA_2MA_{n-1}Pb_nI_{3n+1}$ ($<n>=5$) quasi-2D perovskite films drop-cast on the glass substrate and the PEDOT:PSS coated glass substrate were collected using a UV−Visible spectrophotometer (CARY 50 Bio, Varian). Grazing-incidence wide-angle X-ray scattering (GIWAXS) measurements of the quasi-2D perovskite film drop-cast on the glass substrate were completed at the Shanghai Synchrotron Radiation Facility (SSRF) using the BL16B1 beamline with a photon wavelength of 0.124 nm and a Pilatus 2M CCD as the detector. The incidence light angle was 0.12° and the sample to detector distance was set as 280 mm. A scanning electron microscope (FEI Teneo) was used to obtain the top-view SEM images of the $BA_2MA_{n-1}Pb_nI_{3n+1}$ ($<n>=5$) quasi-2D perovskite film drop-cast on the glass substrate.

STEM characterization

The lamella sample of the $BA_2MA_{n-1}Pb_nI_{3n+1}$ ($<n>=5$) quasi-2D perovskite film with the structure of Glass/Quasi-2D Perovskite/Carbon/Pt was prepared using a FEI Nanolab 200 focused ion beam (FIB) system at the Bio21 Institute Advanced Microscopy Facility. Pt (platinum) protection layers were first deposited using e-beam and then using i-beam on the thin carbon layer coated quasi-2D perovskite film surface as the etching mask. After ion beam etching with 30 keV Ga FIB, the lamella was lifted-off and transferred to the copper grid using an internal micro-manipulator. Several cycles of low keV gentle milling were applied to finally obtain a cross-sectional lamella with ~100 nm thickness (as illustrated in Fig. S2†). The high-angle annular dark-field (HAADF) image and the corresponding STEM-EDAX line scan and elemental mapping of the cross-sectional lamella sample were obtained by a FEI Tecnai TF20 high-resolution transmission electron microscope (TEM).

Photoluminescence (PL) and time-resolved photoluminescence (TRPL) spectroscopy

The PL and the TRPL of the drop-cast $BA_2MA_{n-1}Pb_nI_{3n+1}$ ($<n>=5$) quasi-2D perovskite films were measured through a confocal microscope (Olympus, IX71/FV300), equipped with either a fluorescence spectrometer or a TCSPC setup. The 400 nm excitation beam was the frequency-doubled output of a mode-locked and cavity dumped Ti:Sapphire laser (Coherent Mira900f/APE PulseSwitch, 100 fs FWHM) which was focused on the front surface of films through a 20× objective lens, with the laser spot size estimated to be 1.0×10^{-8} cm^2. The PL emission collected by the same objective lens was filtered by an appropriate highpass filter and detected confocally by a fluorescence spectrometer for obtaining the PL spectra, or by a single photon counting photomultiplier (Becker & Hickl, PMC-100-1) for the TRPL characterizations. TRPL profiles were recorded using a commercial photon counting system (SPC150 card, Becker & Hickl, Germany). The instrument response function of this system is ~200 ps. All signals were collected during a fast scan of the excitation laser over a 10 μm × 10 μm square on the front or back surface of the quasi-2D perovskite films. The 400 nm excitation laser used for PL measurement had a pulse repetition rate of 5.4 MHz and was used with a series of intensities ranging from 0.06 kW/cm^2 to 4.02 kW/cm^2. The laser fluences for TRPL measurements were 1.0 MHz and 0.04 kW/cm^2.

Transient absorption (TA) spectroscopy

Femtosecond pump-probe TA measurements for the $BA_2MA_{n-1}Pb_nI_{3n+1}$ ($<n>=5$) quasi-2D perovskite films spin-coated or drop-cast on the glass substrates were performed using a TA spectrometer at room temperature. The 800 nm pulsed output (96 kHz, 60 fs FWHM) generated by a high repetition rate amplifier (Coherent RegA 9050) was split to generate the pump (525 nm) beam through a tunable optical parametric amplifier (Coherent OPA 9450) and the probe (visible/near-IR white light) beam using a 3-mm-thick sapphire window (CASTECH), respectively. Pump and probe pulses were focused by an off-axis parabolic reflector to overlap at the surface of the film sample with a pump spot size of ~200 μm, giving an excitation fluence of 1.6 μJ·cm^{-2}. Pump induced absorption changes (ΔOD) were measured by comparing adjacent transmitted probe pulses with and without pump pulses using a synchronized mechanical chopper in the path of the pump beam. The time-resolved transient absorption spectra were recorded using a high-speed fiber-optic spectrometer (Ultrafast Systems). The temporal resolution of the setup was estimated to be 200 fs FWHM. The TA spectra of the quasi-2D perovskite film were collected with the pump laser incident from the back side (glass/film) of the film (back-side excitation mode), and also with the pump laser incident from the front side (glass/film) of the film (front-side excitation mode).

Author contributions

K. P. G. supervised the project. F. Z., C. R. H., T. A. S., and K. P. G. wrote the paper with edits from all authors. F. Z., D. A., C. Z., and M. G. prepared the $BA_2MA_{n-1}Pb_nI_{3n+1}$ ($<n>=5$) quasi-2D perovskite films and solar cells. F. Z., C. R. H, S. J. B., and T. A. S. measured the microscopic PL, TRPL, and TA spectra of the quasi-2D perovskite films and analyzed the data. S. R. conducted the SEM and STEM characterization. Z. W. and X. H. conducted the GIWAXS measurements and analyzed the data.

Conflict of Interest

There are no conflicts to declare.

Acknowledgements

Funding support from the ARC Centre of Excellence in Exciton Science (CE170100026) is acknowledged. T. A. S., M. G., D. A. and C. Z. acknowledge support from the Australian Centre for Advanced Photovoltaics (ACAP) program funded by the Australian Government through the Australian Renewable Energy Agency (ARENA), and the Industrial Innovation Program of CSIRO Manufacturing.

References

1. D. H. Cao, C. C. Stoumpos, O. K. Farha, J. T. Hupp and M. G. Kanatzidis, *J. Am. Chem. Soc.*, 2015, **137**, 7843-7850.
2. H. Tsai, W. Nie, J. C. Blancon, C. C. Stoumpos, R. Asadpour, B. Harutyunyan, A. J. Neukirch, R. Verduzco, J. J. Crochet, S. Tretiak, L. Pedesseau, J. Even, M. A. Alam, G. Gupta, J. Lou, P. M. Ajayan, M. J. Bedzyk and M. G. Kanatzidis, *Nature*, 2016, **536**, 312-316.
3. T. M. Koh, V. Shanmugam, X. Guo, S. S. Lim, O. Filonik, E. M. Herzig, P. Müller-Buschbaum, V. Swamy, S. T. Chien, S. G. Mhaisalkar and N. Mathews, *J. Mater. Chem. A*, 2018, **6**, 2122-2128.
4. Y. Lin, Y. Bai, Y. Fang, Q. Wang, Y. Deng and J. Huang, *ACS Energy Lett.*, 2017, **2**, 1571-1572.
5. X. Xiao, J. Dai, Y. Fang, J. Zhao, X. Zheng, S. Tang, P. N. Rudd, X. C. Zeng and J. Huang, *ACS Energy Lett.*, 2018, **3**, 684-688.
6. W. Mao, C. R. Hall, A. S. R. Chesman, C. Forsyth, Y. B. Cheng, N. W. Duffy, T. A. Smith and U. Bach, *Angew. Chem. Int. Ed.*, 2019, **58**, 2893-2898.
7. K. T. Cho, G. Grancini, Y. Lee, E. Oveisi, J. Ryu, O. Almora, M. Tschumi, P. A. Schouwink, G. Seo, S. Heo, J. Park, J. Jang, S. Paek, G. Garcia-Belmonte and M. K. Nazeeruddin, *Energy Environ. Sci.*, 2018, **11**, 952-959.
8. I. C. Smith, E. T. Hoke, D. Solis-Ibarra, M. D. McGehee and H. I. Karunadasa, *Angew. Chem. Int. Ed.*, 2014, **53**, 11232-11235.
9. C. C. Stoumpos, D. H. Cao, D. J. Clark, J. Young, J. M. Rondinelli, J. I. Jang, J. T. Hupp and M. G. Kanatzidis, *Chem. Mater.*, 2016, **28**, 2852-2867.
10. C. M. Mauck and W. A. Tisdale, *Trends Chem.*, 2019, **1**, 380-393.
11. M. D. Smith, B. A. Connor and H. I. Karunadasa, *Chem. Rev.*, 2019, **119**, 3104-3139.
12. Y. Chen, Y. Sun, J. Peng, J. Tang, K. Zheng and Z. Liang, *Adv. Mater.*, 2018, **30**, 1703487.
13. J. Li, J. Wang, J. Ma, H. Shen, L. Li, X. Duan and D. Li, *Nat. Commun.*, 2019, **10**, 806.
14. R. Quintero-Bermudez, A. Gold-Parker, A. H. Proppe, R. Munir, Z. Yang, S. O. Kelley, A. Amassian, M. F. Toney and E. H. Sargent, *Nat. Mater.*, 2018, **17**, 900-907.
15. Z. Wang, Q. Wei, X. Liu, L. Liu, X. Tang, J. Guo, S. Ren, G. Xing, D. Zhao and Y. Zheng, *Adv. Funct. Mater.*, 2020, 31, 2008404.
16. J. Hu, I. W. H. Oswald, S. J. Stuard, M. M. Nahid, N. Zhou, O. F. Williams, Z. Guo, L. Yan, H. Hu, Z. Chen, X. Xiao, Y. Lin, Z. Yang, J. Huang, A. M. Moran, H. Ade, J. R. Neilson and W. You, *Nat. Commun.*, 2019, **10**, 1276.
17. C. M. M. Soe, W. Nie, C. C. Stoumpos, H. Tsai, J.-C. Blancon, F. Liu, J. Even, T. J. Marks, A. D. Mohite and M. G. Kanatzidis, *Adv. Energy Mater.*, 2018, **8**, 1700979.
18. J. Qing, X.-K. Liu, M. Li, F. Liu, Z. Yuan, E. Tiukalova, Z. Yan, M. Duchamp, S. Chen, Y. Wang, S. Bai, J.-M. Liu, H. J. Snaith, C.-S. Lee, T. C. Sum and F. Gao, *Adv. Energy Mater.*, 2018, **8**, 1800185.

19. C. Zuo, A. D. Scully, W. L. Tan, F. Zheng, K. P. Ghiggino, D. Vak, H. Weerasinghe, C. R. McNeill, D. Angmo, A. S. R. Chesman and M. Gao, *Commun. Mater.*, 2020, **1**, 33.
20. J. Liu, J. Leng, K. Wu, J. Zhang and S. Jin, *J. Am. Chem. Soc.*, 2017, **139**, 1432-1435.
21. A. Z. Chen, M. Shiu, J. H. Ma, M. R. Alpert, D. Zhang, B. J. Foley, D. M. Smilgies, S. H. Lee and J. J. Choi, *Nat. Commun.*, 2018, **9**, 1336.
22. Y. Lin, Y. Fang, J. Zhao, Y. Shao, S. J. Stuard, M. M. Nahid, H. Ade, Q. Wang, J. E. Shield, N. Zhou, A. M. Moran and J. Huang, *Nat. Commun.*, 2019, **10**, 1008.
23. T. Luo, Y. Zhang, Z. Xu, T. Niu, J. Wen, J. Lu, S. Jin, S. F. Liu and K. Zhao, *Adv. Mater.*, 2019, **31**, 1903848.
24. M. Yuan, L. N. Quan, R. Comin, G. Walters, R. Sabatini, O. Voznyy, S. Hoogland, Y. Zhao, E. M. Beauregard, P. Kanjanaboos, Z. Lu, D. H. Kim and E. H. Sargent, *Nat. Nanotechnol.*, 2016, **11**, 872-877.
25. T. He, S. Li, Y. Jiang, C. Qin, M. Cui, L. Qiao, H. Xu, J. Yang, R. Long, H. Wang and M. Yuan, *Nat. Commun.*, 2020, **11**, 1672.
26. C. Zuo, A. D. Scully, D. Vak, W. Tan, X. Jiao, C. R. McNeill, D. Angmo, L. Ding and M. Gao, *Adv. Energy Mater.*, 2019, **9**, 1803258.
27. F. Zheng, C. Zuo, M. Niu, C. Zhou, S. J. Bradley, C. R. Hall, W. Xu, X. Wen, X. Hao, M. Gao, T. A. Smith and K. P. Ghiggino, *ACS Appl. Mater. Interfaces*, 2020, **12**, 25980-25990.
28. C. C. Stoumpos, C. M. M. Soe, H. Tsai, W. Nie, J.-C. Blancon, D. H. Cao, F. Liu, B. Traoré, C. Katan, J. Even, A. D. Mohite and M. G. Kanatzidis, *Chem*, 2017, **2**, 427-440.
29. D. Barrit, A. D. Sheikh, R. Munir, J. M. Barbé, R. Li, D.-M. Smilgies and A. Amassian, *J. Mater. Res.*, 2017, **32**, 1899-1907.
30. J. S. Yun, A. Ho-Baillie, S. Huang, S. H. Woo, Y. Heo, J. Seidel, F. Huang, Y. B. Cheng and M. A. Green, *J. Phys. Chem. Lett.*, 2015, **6**, 875-880.
31. F. Zheng, W. Chen, T. Bu, K. P. Ghiggino, F. Huang, Y. Cheng, P. Tapping, T. W. Kee, B. Jia and X. Wen, *Adv. Energy Mater.*, 2019, **9**, 1901016.
32. L. Cabana, B. Ballesteros, E. Batista, C. Magen, R. Arenal, J. Oro-Sole, R. Rurali and G. Tobias, *Adv. Mater.*, 2014, **26**, 2016-2021.
33. J. C. Gonzalez, J. C. Hernandez, M. Lopez-Haro, E. del Rio, J. J. Delgado, A. B. Hungria, S. Trasobares, S. Bernal, P. A. Midgley and J. J. Calvino, *Angew. Chem. Int. Ed.*, 2009, **48**, 5313-5315.
34. Y. C. Kim, N. J. Jeon, J. H. Noh, W. S. Yang, J. Seo, J. S. Yun, A. Ho-Baillie, S. Huang, M. A. Green, J. Seidel, T. K. Ahn and S. I. Seok, *Adv. Energy Mater.*, 2016, **6**, 1502104.
35. S. Chen, X. Wen, J. S. Yun, S. Huang, M. Green, N. J. Jeon, W. S. Yang, J. H. Noh, J. Seo, S. I. Seok and A. Ho-Baillie, *ACS Appl. Mater. Interfaces*, 2017, **9**, 6072-6078.
36. Y. Tian, M. Peter, E. Unger, M. Abdellah, K. Zheng, T. Pullerits, A. Yartsev, V. Sundstrom and I. G. Scheblykin, *Phys. Chem. Chem. Phys.*, 2015, **17**, 24978-24987.
37. G. Xing, B. Wu, X. Wu, M. Li, B. Du, Q. Wei, J. Guo, E. K. Yeow, T. C. Sum and W. Huang, *Nat. Commun.*, 2017, **8**, 14558.
38. Z. Gan, X. Wen, C. Zhou, W. Chen, F. Zheng, S. Yang, J. A. Davis, P. C. Tapping, T. W. Kee, H. Zhang and B. Jia, *Adv. Optical Mater.*, 2019, **7**, 1900971.
39. F. Zheng, X. Wen, T. Bu, S. Chen, J. Yang, W. Chen, F. Huang, Y. Cheng and B. Jia, *ACS Appl. Mater. Interfaces*, 2018, **10**, 31452-31461.
40. J.-C. Blancon, H. Tsai, W. Nie, C. C. Stoumpos, L. Pedesseau, C. Katan, M. Kepenekian, C. M. M. Soe, K. Appavoo, M. Y. Sfeir, S. Tretiak, P. M. Ajayan, M. G. Kanatzidis, J. Even, J. J. Crochet and A. D. Mohite, *Science*, 2017, **355**, 1288-1292.
41. J. Wang, S. Luo, Y. Lin, Y. Chen, Y. Deng, Z. Li, K. Meng, G. Chen, T. Huang, S. Xiao, H. Huang, C. Zhou, L. Ding, J. He, J. Huang and Y. Yuan, *Nat. Commun.*, 2020, **11**, 582.
42. C. Liu, Y. B. Cheng and Z. Ge, *Chem. Soc. Rev.*, 2020, **49**, 1653-1687.